Available online at www.sciencedirect.com

ScienceDirect

Acta Materialia 71 (2014) 255–263

Acta MATERIALIA

www.elsevier.com/locate/actamat

Intra-variant substructure in Ni–Mn–Ga martensite: Conjugation boundaries

B. Muntifering [a,*], R.C. Pond [b], L. Kovarik [c], N.D. Browning [c], P. Müllner [a]

[a] Department of Materials Science and Engineering, Boise State University, Boise, ID 83725, USA
[b] College of Engineering, Mathematics and Physical Sciences, University of Exeter, Exeter EX2 7JL, UK
[c] Environmental Molecular Science Laboratory, Pacific Northwest National Laboratory, PO Box 999, Richland, WA 99352, USA

Received 14 November 2013; received in revised form 6 March 2014; accepted 9 March 2014
Available online 12 April 2014

Abstract

The microstructure of a Ni–Mn–Ga alloy in the martensitic phase was investigated using transmission electron microscopy. Inter-variant twin boundaries were observed separating non-modulated tetragonal martensite variants. In addition, intra-variant boundary structures, referred to here as "conjugation boundaries", were also observed. We propose that conjugation boundaries originate at the transformation interface between austenite and a nascent martensite variant. In the alloy studied, deformation twinning was observed, consistent with being the mode of lattice-invariant deformation, and this can occur on either of two crystallographically equivalent conjugate $\{1\,0\,1\}\langle 1\,0\,\bar{1}\rangle$ twinning systems: conjugation boundaries separate regions within a single variant in which the active modes were distinct. The defect structure of conjugation boundaries and the low-angle of misorientation across them are revealed in detail using high-resolution microscopy. We anticipate that the mobility of such boundaries is lower than that of inter-variant boundaries, and is therefore likely to significantly affect the kinetics of deformation in the martensitic phase.

Keywords: Ni–Mn–Ga; Martensite interface; HRTEM; Twin boundary; Disconnection

1. Introduction

Ferromagnetic shape memory alloys, such as Ni_2MnGa [1,2], are promising candidates for sensor and actuator applications due to their large strain and fast response. The magnetic and mechanical properties of these materials directly depend on the microstructure [3–7], which, in turn, is determined by the relative ease of heterogeneous nucleation vs. growth of the daughter variants produced by transformation from the parent phase. The number of crystallographically equivalent variants follows from Lagrange's theorem, i.e. it is equal to the ratio of the orders of the parent and daughter point groups. In the present study, the martensite exhibited tetragonal symmetry, $4/m\,mm$ (order 16), so only three variants arise since the parent symmetry is cubic, $m\bar{3}m$ (order 48) [8]. Thus, when transformation is complete, the microstructure is expected comprise the three variants, separated by inter-variant boundaries [9]. However, we show in this work that variants actually exhibit a substructure of domains. Moreover, we present transmission electron microscopy (TEM) images revealing the atomic-scale structure of domain boundaries, and show that they originate because of prolific mechanical twinning on conjugate systems within variants of such relatively high symmetry. Consequently, we designate the domain boundaries "conjugation boundaries".

* Corresponding author.
E-mail address: brittanymuntifering@u.boisestate.edu (B. Muntifering).

http://dx.doi.org/10.1016/j.actamat.2014.03.018
1359-6454/

2. Conjugate twinning systems

The microstructure of the martensite phase forms as a result of a temperature-induced self-accommodating martensitic transformation [9]. For a cubic-to-tetragonal transformation, the martensite variants formed within one initial grain belong to three symmetry-equivalent orientations of the tetragonal c direction, as depicted in Fig. 1a. These are interrelated by $\{1\,1\,0\}_A$ mirror planes of the austenite; one example is indicated in Fig. 1a. (For simplicity, we have chosen face-centered tetragonal (fct) cells. The conventional choice would be the body-centered cell rotated by 45° about [0 0 1] with respect to the face-centered cell [10]. Also, we omit the subscript when referring to the fct axis system.) We focus on a single martensite variant, designated M in Fig. 1a, which is shown enlarged in Fig. 1b. Mechanical twinning can occur on {1 0 1) planes with twinning direction $\langle 1\,0\,\bar{1}]$ in this variant: these four twinning systems can be subdivided into two conjugate pairs with twinning planes (1 0 1) and $(\bar{1}\,0\,1)$, and (0 1 1) and $(0\,\bar{1}\,1)$. The former pair is illustrated in Fig. 1b. Using the terminology of mechanical twinning [11], (1 0 1) is the K_1 plane and $[1\,0\,\bar{1}]$ is the η_1 direction of this compound twin, which is shown in red, and $(\bar{1}\,0\,1)$, $[\bar{1}\,0\,\bar{1}]$ is the conjugate system in blue (K_2, η_2). Consequently, we designate these conjugate systems T_1 and T_2 in the present work. We note that the conjugate systems (1 0 1) and $(\bar{1}\,0\,1)$ are interrelated by the (1 0 0) mirror plane which is aligned with the $(1\,0\,0)_A$ mirror plane in austenite, Fig. 1a. Thus, the conjugate twinning systems T_1 and T_2 occur on crystallographically equivalent planes in the tetragonal cell.

We define the following angles for use in later discussion. The acute angle, ψ_0, between the K_1 and K_2 planes is given by $\psi_0 = 2\tan^{-1}(a/c)$: using the tetragonal lattice parameters at the martensitic transformation temperature (Section 3.1), $\psi_0 = 80.45°$. The angle between K_1 and [1 0 0] is designated θ, and can be expressed as $\theta = 90 - \psi_0/2 = 49.78°$. Also, the misalignment of the [1 0 0] directions in T_1 and T_2, labeled δ_0 in Fig. 1b, is equal to $\delta_0 = 2\theta - \psi_0 = 19.10°$.

In previous work [12–14] it has been demonstrated that twinning on these systems proceeds by the motion of disconnections along the twin boundaries. For the T_1 system, the Burgers vector of the disconnections is very close to $\boldsymbol{b}^d = 1/12[1\,0\,\bar{1}]$, and the step height is $h = d_{(2\,0\,2)}$, where $d_{(2\,0\,2)}$ is the interplanar spacing of (2 0 2) planes. Similarly, for the T_2 system, $\boldsymbol{b}^d = 1/12[\bar{1}\,0\,\bar{1}]$, and the step height is $h = d_{(\bar{2}\,0\,2)}$. The shear for both systems is equal to $|\boldsymbol{b}^d|/h = c/a - a/c$, which has the magnitude 0.36 in the present case.

3. Experimental procedure

3.1. Sample preparation

Two samples were prepared for TEM analysis. The first was polycrystalline $Ni_{46.75}Mn_{34}Ga_{19.25}$ (at.%), which was prepared in a Reitel induction furnace from the constitutive metals Ni 99.9% (Alfa Aesar), Mn 99.9% (Alfa Aesar) and Ga 99.999% (Sigma Aldrich) and cast into a copper mold. The purity levels quoted specify only metallic impurity concentrations. The crystal structure of the bulk polycrystalline sample was analyzed using a Bruker D8 diffractometer with Cu Kα radiation. At room temperature, the structure was non-modulated tetragonal with lattice parameters $a = b = 5.50 \pm 0.02$ Å and $c = 6.58 \pm 0.04$ Å. Subsequently, the sample was heated in the diffractometer until austenite peaks could be seen. At the transformation temperature, the tetragonal lattice parameters were $a = b = 5.54 \pm 0.02$ Å and $c = 6.55 \pm 0.04$ Å and the austenite lattice parameter was $a_A = 5.86 \pm 0.02$ Å.

The second sample was a single crystal with composition $Ni_{53.4}Mn_{25.9}Ga_{20.7}$, which was grown by the Bridgman method using ultrapure Mn (99.9997%) with less than 100 ppm oxygen (Institute of Physics Polish Academy of Sciences) in an argon–6% hydrogen atmosphere. The crystal was heat treated at 950 °C for 48 h followed by 750 °C for 12 h in an argon atmosphere [15]. A slice was cut from the center of the single crystal and energy-dispersive X-ray spectroscopy was performed, which showed a composition

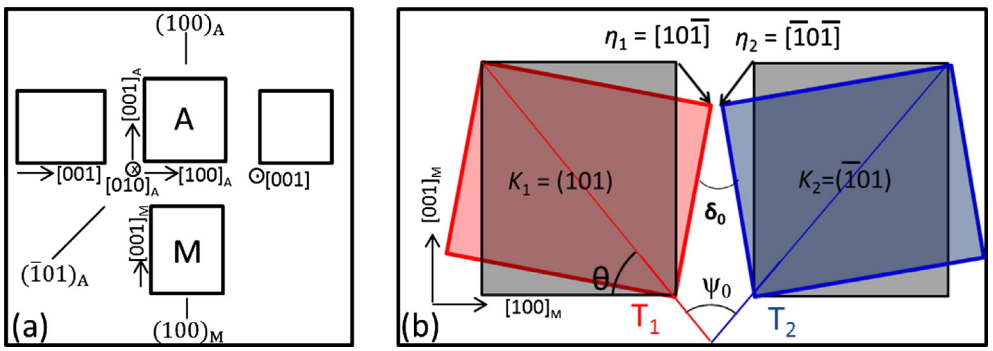

Fig. 1. (a) Three tetragonal variants form as a result of a martensitic transformation and are interrelated through the $\{1\,1\,0\}_A$ mirror planes of the parent phase (A). (b) Variant M (black) and twinning on conjugate systems (red and blue). (For interpretation of the references to color in this figure legend, the reader is referred to the web version of this article.)

of $Ni_{53.5}Mn_{24.9}Ga_{21.6}$. X-ray diffraction confirmed a non-modulated structure.

TEM specimens were prepared from slices of both samples. Slices were mechanically thinned to 80–120 μm and discs with a diameter of 3 mm were obtained using a punch (model 656 Gatan, Inc.). Thin foils were then prepared in a TenuPol 3 (Struers) double-jet electropolisher operated at 243 K and 10 V using an electrolyte of 700 ml methanol (Aldrich) and 300 ml 69.9 vol.% nitric acid (Aldrich).

4. TEM observations

The polycrystalline foils were examined at room temperature in a JEOL 2100 HR TEM operated at 200 kV with a LaB_6 filament. The single crystal foils were studied with high angle annular dark-field (HAADF) scanning transmission electron microscopy (STEM) using an FEI Titan 80-300 instrument with c_s-correction operated at 300 kV at Pacific Northwest National Laboratory.

The structure of a conjugation boundary separating two domains is shown at relatively low magnification and viewed along in [0 1 0] Fig. 2a. Each domain was a composite configuration comprising parallel twins in variant M. In the left-hand domain the twinning system was T_1, so we designate this domain (M^+, T_1), and, similarly, the right-hand domain was (M^-, T_2): the "+" and "–" superscripts indicate that the left-hand domain was rotated anti-clockwise about [0 1 0] by a small angle, $\varphi/2$, and the other clockwise by $\varphi/2$. Three features of Fig. 2a are of interest: the magnitude of the angular misorientation of adjacent domains, φ, the twinning fraction, f, in each domain and the defect structure along the boundary. These aspects are discussed separately below.

4.1. Domain misorientation, φ

The selected area diffraction pattern from each domain is inset in its corresponding domain in Fig. 2a. Fig. 2b shows the diffraction pattern recorded when the aperture straddled both domains. These diffraction patterns demonstrate that the two domains were formed of the same martensite variant, M, and that the twinning system in the left-hand domain was T_1 with K_1 parallel to (1 0 1), while that in the right-hand domain was T_2 with K_2 parallel to $(\bar{1}\,0\,1)$. The (0 0 4) planes on the left and right side of the boundary were misoriented by $\varphi = 7° \pm 1°$, as indicated by the diffraction spots 004_{M^+} and 004_{M^-} in Fig. 2b. The misorientation φ was also evident from the angle between K_1 and K_2 in the two domains, designated ψ in Fig. 2a. This angle was $88° \pm 1°$, differing from the angle ψ_0 calculated in Section 2 by $7.55° \pm 1°$, i.e. consistent with being equal to $\psi = \psi_0 + \varphi$ within experimental error. Thus, as a result of the misorientation, φ, between M^+ and M^- being introduced, the initial misalignment of T_1 and T_2 has been reduced from δ_0 to $\delta = \delta_0 - \varphi = 12.10° \pm 1°$: this is the angle between the diffraction spots $(400)_{T_2}$ and $(400)_{T_1}$ in Fig. 2b.

4.2. Twinning fraction, f

The dark-field image of domain (M^-, T_2) in Fig. 3a was formed using the reflection $\mathbf{g} = 202_{T2}$, where the subscript indicates indexing with respect to the twinned crystal. Both domains were aligned along [0 1 0] with the twin boundaries oriented edge-on: the twin widths were finest near the conjugation boundary. Fig. 3b is a bright-field image of the same area, but with domain (M^-, T_2) tilted to a two-beam

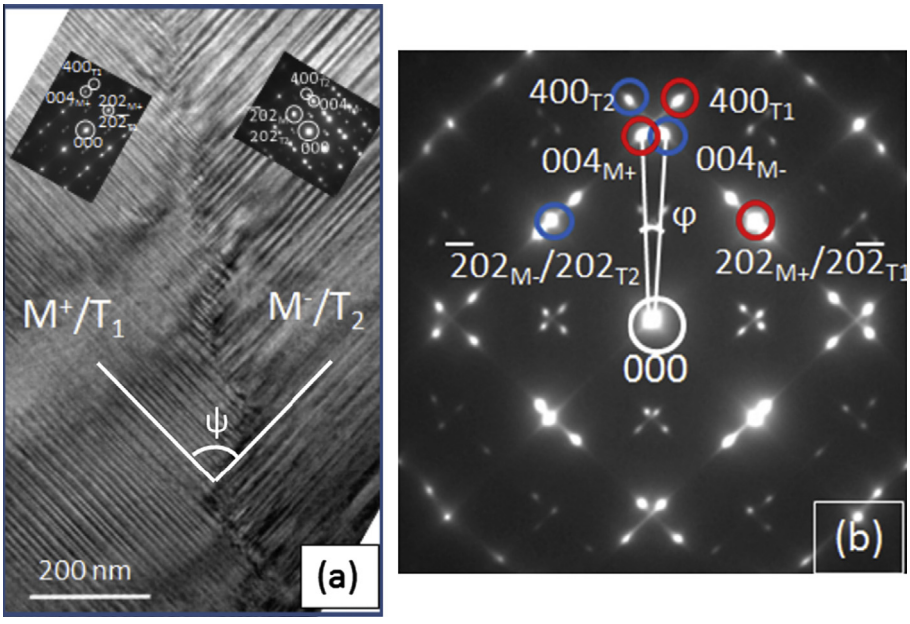

Fig. 2. (a) Conjugation boundary imaged along the [0 1 0] zone axis. The insets are diffraction patterns of domains M^+/T_1 (left) and M^-/T_2 (right). (b) Diffraction pattern over both domains aligned along [0 1 0] zone axis. The 0 0 4 reflections from M^+ and M^- are inclined at an angle of $\varphi = 7° \pm 1°$.

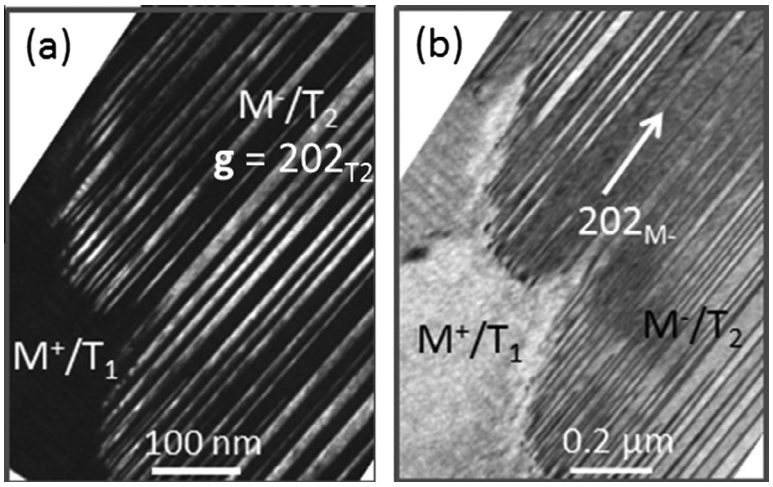

Fig. 3. (a) Dark-field image with both domains aligned along the [0 1 0] zone axis, and with the aperture displaced to select the 202_{T2} reflection. (b) Bright-field image with the M^-/T_2 domain tilted into a two beam condition with $\mathbf{g} = 202_{M-}$.

condition with $\mathbf{g} = 202_{M-}$, showing that the twin widths coarsened progressively with distance from the interface. Additional observations indicated that the extent of coarsening was less in domain (M^+, T_1).

Image analysis software was used on the dark-field image in Fig. 3a. A Hough transformation was applied to the image for line extraction to identify the twin boundary locations. These lines were smoothed with directional average filtering and adaptive thresholding was then applied to create a binary image of the twins. The ratio of the twin-matrix thicknesses, f, was determined as the ratio of white to black pixels. This procedure was carried out with edge-on dark-field images, such as Fig. 3a, from both domains. The twinning fraction, f, was 0.38 ± 0.05 in both domains.

4.3. Defect structure

Fig. 2a shows that the conjugation boundary exhibited facets, the largest being ~100 nm in length. These facets had both "symmetrical" and "asymmetrical" orientations. Asymmetrical facets were nearly parallel to the twin planes in the two domains, while the symmetrical facets were oriented close to $(1\,0\,0)_A$, i.e. symmetrically disposed between $(1\,0\,0)_{M^+}$ and $(1\,0\,0)_{M^-}$.

Fig. 4a is a dark-field image showing the conjugation boundary with the sample tilted ~5° off the [0 1 0] axis so that the (M^+, T_1) domain was in a common two-beam condition with $\mathbf{g} = 202_{M+}/20\bar{2}_{T1}$. Thus, both M^+ and T_1 appear with the same contrast and the twin boundaries separating them were invisible, whereas the boundaries between M^- and T_2 remain visible. Fig. 4b is a magnified image of the area indicated within the box in Fig. 4a. Alternating black and white contrast lobes were observed along the conjugation boundary, emanating from the terminations of twins in the (M^-, T_2) domain and extending into the (M^+, T_1) domain. Fig. 4c is a schematic representing this contrast feature as a sequence of bright and dark ovals.

Fig. 5a is a HAADF STEM image of the single crystal sample viewed along the [0 1 0] direction. The atomic resolution image clearly displays the presence of twins in the microstructure: however, the location and the character of the twinning disconnections are not immediately evident based on a casual inspection. In order to visually enhance the presence of disconnections, we have performed a centro-symmetry analysis for all atomic columns identified in the image, and color-coded the images according to this parameter [16]. The color-coded image is presented in Fig. 5b. Blue represents sites with a high degree of centro-symmetry, while warmer colors represent sites with a broken centro-symmetry, such as those at twin boundaries. Consequently, steps along the twin boundaries can be readily identified as disconnections. In Fig. 5b, the matrix is labeled M and the twin is labeled T. This image reveals disconnections viewed end-on in the twin boundary. Previous work [12–14] used alpha-fringe contrast to characterize the disconnections [17] and the Burgers vector and step height deduced in that work, $\boldsymbol{b}^d = 1/12[10\bar{1}]$ and $h = d_{(202)}$, respectively, can be confirmed directly from this image by circuit mapping [18]. The area indicated by a white box in Fig. 5b is magnified in Fig. 5c, showing that T is two $d_{(202)}$ planes thick at the left side and tapers to the right in two discrete steps, as demonstrated schematically in Fig. 5d. The matrix is colored blue, and grey lines, represent $(50\bar{7})_M/(507)_T$ planes, which are straight and parallel in the twin and matrix, except where strongly distorted near defect cores.

Fig. 6a is a HAADF STEM image of a conjugation boundary viewed along [0 1 0], and Fig. 6b is the corresponding color-coded image. This structure resembles that seen in Fig. 2a, except that this conjugation boundary exhibited symmetric and, predominantly, asymmetric micro-facets. Fig. 6c schematically depicts the reactions of disconnections originating from the T_1 and T_2 twinning systems as they impinge. Six disconnection interactions, numbered 1–6, were observed: 1–2 correspond to a symmetrical interaction,

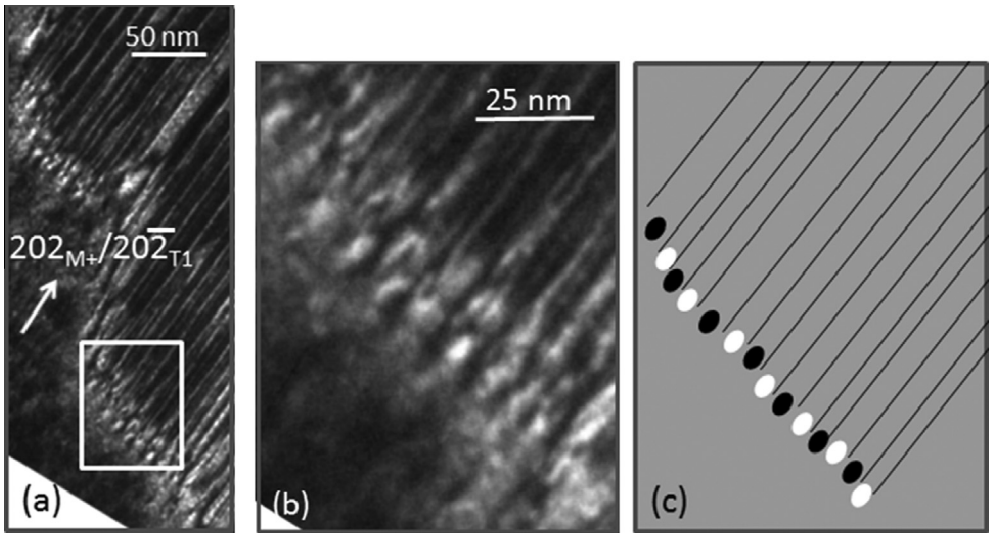

Fig. 4. (a) Dark-field image of the conjugation boundary, with the M^+/T_1 domain in the two beam condition $\mathbf{g} = 202_{M+}/20\bar{2}_{T1}$. (b) Magnified image of the boxed area in (a). (c) Schematic illustration depicting the alternating black and white contrast.

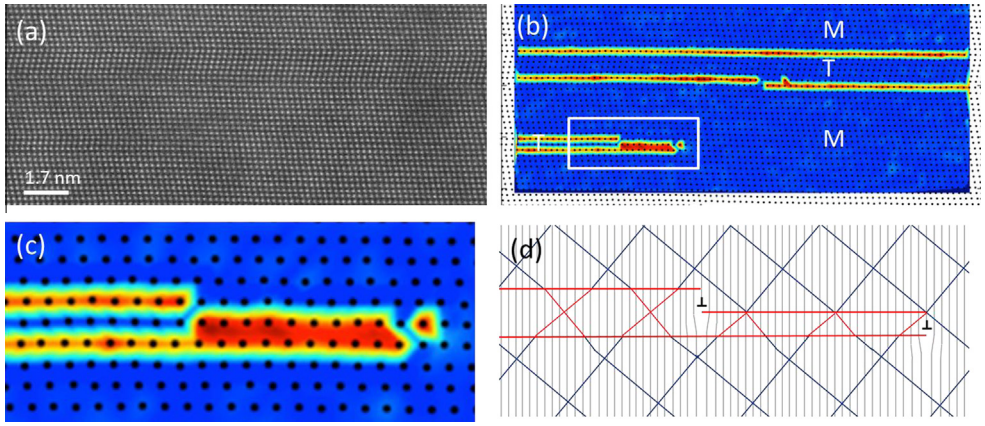

Fig. 5. (a) HAADF STEM image viewed along [010]. (b) Color-coded image from (a), where blue represents atomic columns with perfect tetragonal symmetry and warmer colors show deviation from this. (c) Magnified view of area boxed in (b). (d) Schematic illustration of (c) depicting twinning disconnections. Matrix (M) is blue, with the red twin variant (T) terminating after two twinning disconnections. The gray lines represent the $(50\bar{7})_M$ planes. (For interpretation of the references to color in this figure legend, the reader is referred to the web version of this article.)

and 3–6 correspond to T_2 disconnections blocked at a T_1 barrier, resulting in an asymmetrical facet.

5. Discussion

The observations presented in Section 4 are consistent with the model of formation of conjugation boundaries depicted schematically in Fig. 7. The variant M nucleates heterogeneously with nominal habit plane $(011)_A$ [19] and $\{101\}/\langle 10\bar{1}]$ twinning ensues as the mode of lattice-invariant deformation (LID) [20]. At one location, in the domain on the left of Fig. 7, the T_1 twinning mode is operative, while at another location, in the domain on the right of the diagram, the conjugate system T_2 ensues. Consequently, in the wake of the inter-phase boundary as it advances into the austenite, a conjugation boundary forms where the domains impinge. These martensitic domains are interrelated by a $(100)_A$ mirror plane. Three features of this model are considered in greater depth in the following sections. The first feature is the magnitude of the domain misorientation, φ. This misorientation originates from the extent of LID twinning which is induced in the martensite plates to remove coherency strains between the two phases [20]. An ancillary consequence of such misfit removal is that a small angular misorientation, $\varphi/2$, arises between the phases, so that the eventual misorientation at the conjugation boundary is φ. In Section 5.1 we show how φ can be estimated. The second feature is the configuration of dislocations along conjugation boundaries, and this is discussed in Section 5.2. Finally, in Section 5.3, we explain why conjugation boundaries are constituted predominantly of asymmetric facets, rather than symmetric ones, despite the expectation that the latter have distortion fields with smaller stored elastic energy.

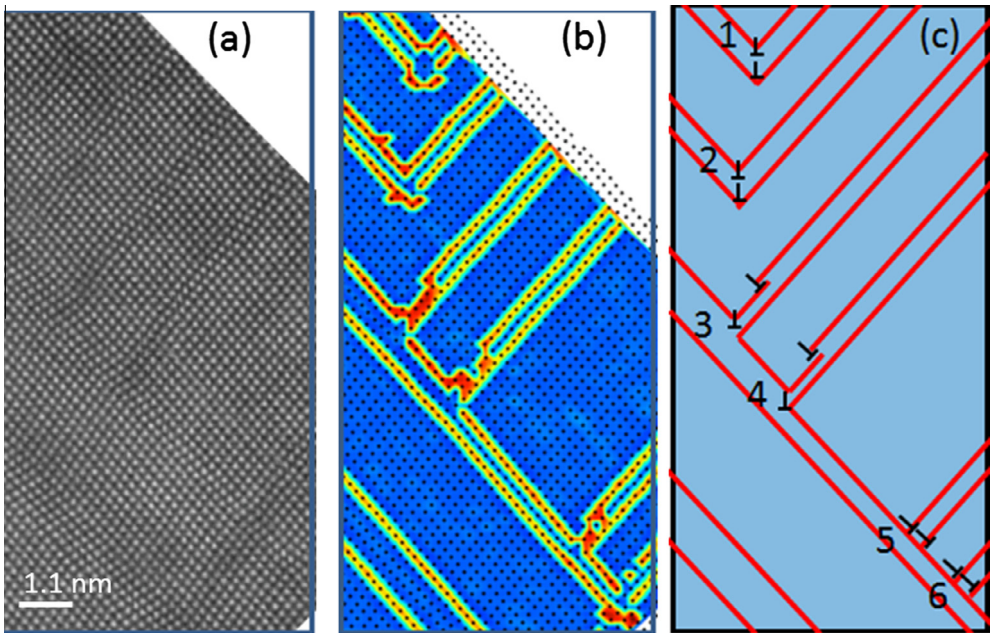

Fig. 6. (a) HAADF STEM image of a conjugation boundary. All twins are viewed along [010]. (b) Corresponding color-coded image. (c) Defect configuration at the interface: six T_1/T_2 twin interactions are present and labeled 1–6.

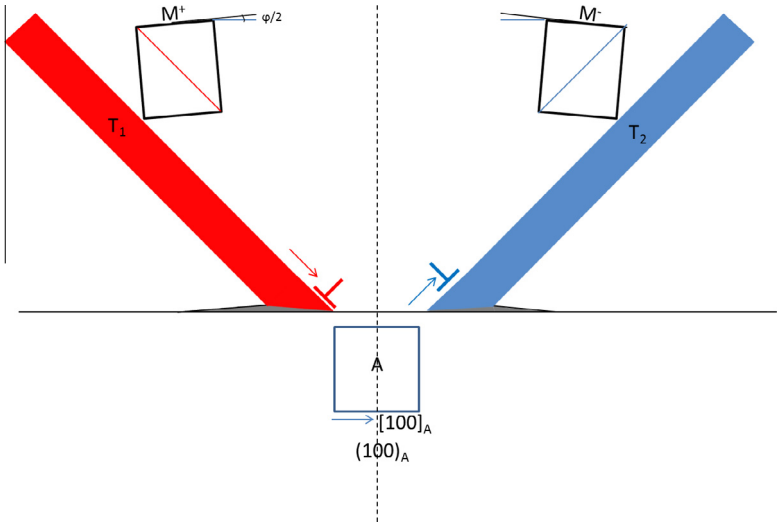

Fig. 7. Schematic illustration of the accommodation of misfit at a $(0\,1\,1)_A$ habit plane between austenite (lower crystal) and martensite (upper crystal). The lattice-invariant deformation mode is twinning on the T_1 system in the left-hand domain, and T_2 in the right-hand domain. The vertical dashed line represents the eventual location of a conjugation boundary.

5.1. Estimation of φ

Consider the misfit along $[1\,0\,0]_A$ in the interface depicted in Fig. 7. The true misfit parameter at a coherent interface depends on (1) the ratio of elastic moduli of the austenite and martesnite phases [21] and (2) the true strain and not the engineering strain [22]. Around the martensite–austenite transition, the elastic constants depend rather strongly on temperature and both phases are strongly anisotropic [23,24]. However, a detailed treatment of elastic anisotropy is beyond the scope of this work. In the approximation of homogeneous, isotropic, linear elasticity, the strain in the austenite and martensite phases is equal and opposite and the difference between engineering strain and true strain is negligible. Initially, $[1\,0\,0]_M$ is aligned with $[1\,0\,0]_A$, and the resulting misfit, ε^m, along this direction is equal to $\varepsilon^m = 2(a_A - a_m)/(a_A + a_m)$: using the lattice parameters determined by XRD at the transformation temperature, ε^m is equal to 5.61%. The inception of mechanical twinning relieves this misfit strain in the growing martensite plate [25]. The mechanism is the motion of twinning disconnections along the twin interfaces, either from a source within the martensite plate or nucleated at the austenite–martensite interface. Whichever mechanism operates, interfacial dislocations, with Burgers vector equal to $\boldsymbol{b}^d$, arise at the austenite–martensite interface, as depicted

schematically in Fig. 7. In Fig. 7, the twins are shown schematically as though they emerge at a free surface of the martensite: in fact, the interfacial gaps shown as gray shaded areas in Fig. 7 would be closed, giving rise to a short-range distortion field. Let the component of the Burgers vector which is parallel to the austenite–martensite interface be designated $\boldsymbol{b}^d_{//} = \boldsymbol{b}^d \cos\theta$, and that perpendicular to the interface be $\boldsymbol{b}^d_{\perp} = \boldsymbol{b}^d \sin\theta$: at the transformation temperature their values are 0.462 Å and 0.546 Å, respectively. An array of such dislocations with appropriate spacing along the interface can accommodate the misfit (by virtue of the components $\boldsymbol{b}^d_{//}$), but also produces a misorientation $\varphi/2$ (by virtue of the components $\boldsymbol{b}^d_{\perp}$). We note that the $\boldsymbol{b}^d_{//}$ components have the same sign in both domains, whereas the $\boldsymbol{b}^d_{\perp}$ components have opposite sign. Thus, both twinning modes can accommodate the misfit present, but give rise to misorientations with opposite sign, as indicated in Fig. 7.

For simplicity, we assume that these dislocations are dispersed individually and are equi-spaced along the interface, whereas, in fact, they are grouped together, as in Fig. 7, on adjacent (2 0 2) planes, forming narrow twins. The spacing between individual dislocations necessary to relieve misfit, L, and the misorientation, $\varphi/2$, can be determined following the method described by Hirth and Pond [22]: this iterative procedure takes into account the non-linear change of the magnitudes of $\boldsymbol{b}^d_{//}$, and $\boldsymbol{b}^d_{\perp}$ as the misorientation accrues. Two equations are employed (with signs appropriate for this case):

$$\varepsilon^m = \left[b^d_{//} + b^d_{\perp}\tan(\varphi/4)\right]/L_0 \approx b^d_{//}/L_0 \tag{1}$$

and Frank's relation:

$$\varphi/2 = 2\sin^{-1}\left(b^d_{\perp}/2L_0\right) \approx b^d_{\perp}/L_0 \tag{2}$$

where the approximate forms would be accurate in the limit of small φ. L_0 is estimated from the approximate form in Eq. (1), and φ is determined from the exact form in Eq. (2). This value of φ is substituted into the exact form of Eq. (1) to give an updated value L, and iteration proceeds. The convergence is rapid because of the weak dependence of φ on L_0. In the present case, the initial values are $L_0 = 8.24$ Å and $\varphi_0/2 = 3.80°$, and the final values are $L = 8.53$ Å and $\varphi/2 = 3.67°$. The increment in L reflects the fact that the sense of φ enlarges the component of $\boldsymbol{b}^d$ parallel to the equilibrium interface plane, while the decrement in $\varphi/2$ arises because the component of $\boldsymbol{b}^d$ perpendicular to the interface diminishes and the defect spacing increases. As a consequence, when impingement of domains (M^+, T_1) and (M^-, T_2) occurs, the adjacent domains are expected to be misoriented by $\varphi = 7.33°$ about [0 1 0], which is in good agreement with the measured value of $7° \pm 1°$. We note that the value of φ is much larger in the present case than commonly found in phase transformations, typically <1° [22,25]. This is a consequence of the large value of $\boldsymbol{b}^d_{\perp}$, which does not contribute to misfit accommodation, which, furthermore, is a testament to the low energy and ease of nucleation of twinning in this alloy [12]. (In a fuller treatment of the austenite–martensite interface structure it is necessary to consider the line direction of the twinning disconnections and the contribution of a further array of transformation disconnections to misfit accommodation [25]. However, these contributions are small parallel to [1 0 0].)

The twinning fraction can be expressed as

$$f = \frac{d_{(2\,0\,2)}}{L\cos(\theta - \varphi/2)} \tag{3}$$

which has the value 0.36 in the present case, which is in good agreement with the measured value of 0.38 ± 0.05.

5.2. Defect structure of conjugate boundaries

Two principal types of disconnection interactions occur where the twinning systems T_1 and T_2 meet. The first type of interaction, as at sites 1 and 2 in Fig. 6, is schematically depicted in Fig. 8a. Here, a twinning disconnection of system T_1 with Burgers vector $\boldsymbol{b}^d_1$ meets a twinning disconnection of system T_2 with Burgers vector $\boldsymbol{b}^d_2$ and reacts to form a "grain boundary" dislocation [26] with magnitude $\boldsymbol{b}^g = 2\boldsymbol{b}^d\sin(\psi/2)$, which is oriented parallel to $[1\,0\,0]_A$. According to Frank's rule, this reaction is energetically favorable if $\boldsymbol{b}^g < \sqrt{2}\boldsymbol{b}^d$: as shown schematically in Fig. 8, this is the case since $\psi < 90°$. A wall of such dislocations creates a symmetrical tilt boundary with modest stored elastic energy.

The second type of interaction, as at sites 5 and 6 in Fig. 6c, occurs when incident disconnections of system T_2 encounter a T_1 twin, forming a wall at the T_1 barrier, Fig. 8b. This defect arrangement constitutes a local energy minimum and is metastable (i.e. not in equilibrium) and results in an asymmetrical facet. The component of $\boldsymbol{b}^d_2$ perpendicular to the T_1 twin boundary is $\boldsymbol{b}^d_2\sin(\psi) = 0.714$ Å, and the small component parallel to the interface is $\boldsymbol{b}^d_2\cos(\psi) = 0.025$ Å. Fig. 4a was taken with $\boldsymbol{g} = 2\,0\,2_{M+}/2\,0\,\bar{2}_{T1}$ and shows contrast consistent with the stress field of such defect walls: the black/white lobe contrast in Fig. 4 extends into the M^+/T_1 domain to a distance which corresponds to the thickness of the twins in the M^-/T_2 domain at the interface. Here, the width of the T_2 twins is of the order of 10 nm, i.e. much larger than in Fig. 6. In-plane Burgers vector components, $\boldsymbol{b}^d_i\cos(\psi)$, would generate a long-range stress field. However, if, overall, there are equal areas of the two orientations of asymmetric facets, as observed experimentally in e.g. Fig. 2, these stresses would cancel at long distance, thereby reducing the strain energy of the conjugation boundary.

It can be advantageous to model such defect arrays as a disclination dipole array, as illustrated in Fig. 9. This approach significantly reduces the numerical effort when calculating the stress field [27,28], albeit by neglecting the small in-plane component of the Burgers vectors at the asymmetrical facets. Such an approach is appropriate in situations where the stresses of the asymmetrical facets

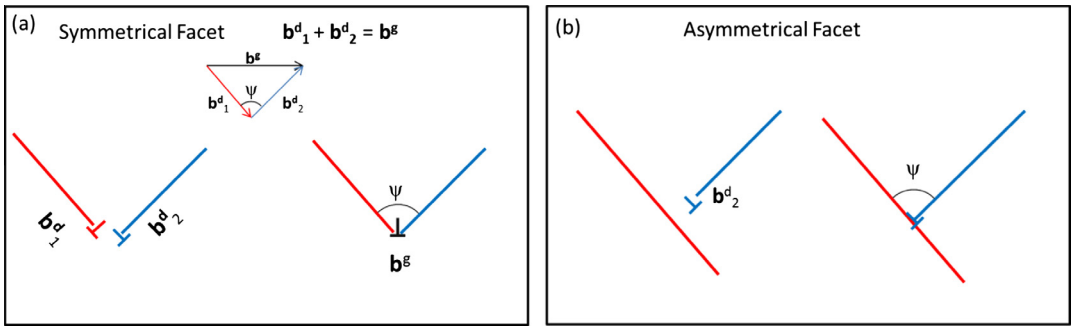

Fig. 8. Schematic illustration of twinning disconnection interactions at symmetric (a), and asymmetric (b) facets of a conjugation boundary.

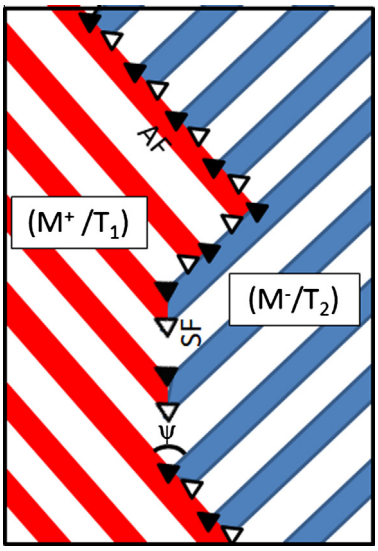

Fig. 9. Disclination dipole representation of the defect structure at symmetric (SF) and asymmetric facets (AF) of a conjugation boundary.

are small and cancel at relatively short distance. While compromising accuracy of the strain fields, a disclination approach predicts the misorientations produced by certain hierarchical defect arrangements comprising large numbers of dislocations and disconnections [29]. A similar approach has been taken to model the defect content of the film/substrate interfaces of epitaxially grown thin films of twinned ferroelectric systems [30–32]. In those cases, the Burgers vectors of twinning dislocations had large components parallel to the substrate/film interface and were modeled as Somigliana dislocation dipoles.

5.3. Predominance of asymmetric facets

Symmetric facets have no Burgers vector content parallel to the interface and are therefore energetically more favorable than asymmetric ones. Thus, symmetric facets would be expected to dominate at equilibrium. However, Figs. 2 and 6 show that asymmetrical facets actually dominate. We suggest that this arises for kinetic reasons associated with the stochastic occurrence of the two twinning modes at austenite–martensite interfaces. In order to form an entirely symmetrical conjugation boundary, each pair of abutting twins from domains (M^+, T_1) and (M^-, T_2) would have to exhibit the same thickness and meet in registry. This improbable mechanism is depicted schematically in Fig. 10a, where dashed black lines represent {202} planes in the twins of the adjacent domains and both domains have a twinning fraction of 0.4. A less symmetrical but more probable arrangement, leading to the formation of a mixture of symmetric and asymmetric facets, is illustrated in Fig. 10b. Here, the twinning fraction is the same as above, but the twin widths are different in each domain so only partial registry occurs. In Fig. 10c the twin widths are again different and meet without registry so that only asymmetric facets form.

Conjugation boundaries are likely to affect the kinetics of shape deformation in response to an applied stress or magnetic field. Because of their complex structures and low energies, we anticipate that their mobility is likely to be lower than that of inter-variant boundaries, and in situ TEM observations are currently in progress to establish the mechanism of motion.

In conventional treatments of martensitic microstructures [9], only the three tetragonal variants are considered. These are relatively disposed so that their mutual interfaces are consistent with the notion of kinematic compatibility, or, alternatively expressed, as invariant plane interfaces. However, the present work demonstrates that further mechanistic considerations may be necessary. The conjugation boundaries observed here are thought to have arisen through the mechanism of stress accommodation at austenite–martensite interfaces: mechanical twinning is proposed as the active mode of lattice-invariant deformation, and introduces ancillary tilting by the angle φ between intra-variant domains. It is on the basis of this mechanism that the authors choose to use the terminology of deformation twinning, in addition to the generic term "transformation twinning" widely used in this field. Of course, this mechanism does not violate the fundamental principle of symmetry conservation encapsulated by the Lagrange expression [8]. The two domains shown in Fig. 2, for example, are interrelated by a $(100)_A$ mirror plane. Ni–Mn–Ga alloys with other compositions exhibit monoclinic symmetry [33]. In such cases, more variants arise, but conjugation boundaries may be avoided because conjugate twin planes may not be crystallographically equivalent.

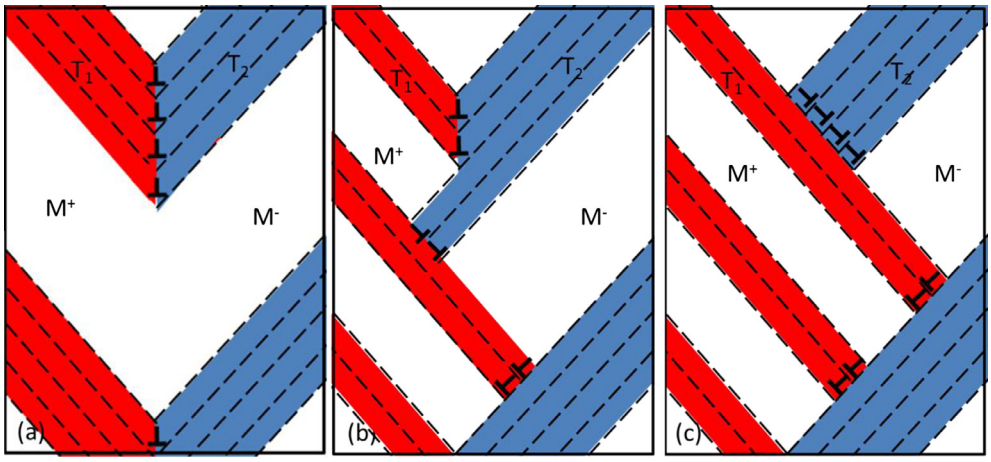

Fig. 10. Schematic illustration of the formation of symmetric and asymmetric facets: (a) entirely symmetric conjugation boundary requiring twins of equal width to meet in registry, (b) mixed symmetric and asymmetric facets and (c) entirely asymmetric facets.

6. Summary

We have identified a microstructural feature which arises in the non-modulated martensitic phase of a Ni–Mn–Ga alloy. These "conjugation boundaries" were observed within tetragonal variants of the martensitic phase, and are formed where domains of $(1\,0\,1)[1\,0\,\bar{1}]$ and $(\bar{1}\,0\,1)/[\bar{1}\,0\,\bar{1}]$ conjugate deformation twins impinge. We attribute this intra-variant substructure to two primary factors. First, the variants exhibit relatively high symmetry, $4/m\ mm$, so that lattice-invariant deformation can occur on conjugate twinning systems. Second, these modes of twinning are very easily induced.

Acknowledgments

We thank Nikki Kucza and Martika Flores-Ramos for assistance with the growth of single crystals. We acknowledge partial financial support from the National Science Foundation through Grant DMR-1008167, and NSF MRI awards 0521315 (TEM) and 0619795 (XRD). The research described in this paper is part of the Chemical Imaging Initiative at Pacific Northwest National Laboratory under Contract DE-AC05-76RL01830 operated for the Department of Energy by Battelle. A portion of the research was performed using EMSL, a national scientific user facility sponsored by the Department of Energy's Office of Biological and Environmental Research and located at Pacific Northwest National Laboratory.

References

[1] Ullakko K, Huang JK, Kantner C, Ohandley RC, Kokorin VV. Appl Phys Lett 1996;69:1966.
[2] Soderberg O, Ge Y, Sozinov A, Hannula SP, Lindroos VK. Smart Mater Struct 2005;14:S223.
[3] Chmielus M, Rolfs K, Wimpory R, Reimers W, Müllner P, Schneider R. Acta Mater 2010;58:3952.
[4] Chmielus M, Chernenko VA, Knowlton WB, Kostorz G, Müllner P. Eur Phys J-Spec Top 2008;158:79.
[5] Heczko O, Straka L, Seiner H. Acta Mater 2013;61:622.
[6] Straka L, Hanninen H, Lanska N, Sozinov A. J Appl Phys 2011;109.
[7] Straka L, Lanska N, Ullakko K, Sozinov A. Appl Phys Lett 2010;96.
[8] Webster PJ, Ziebeck KRA, Town SL, Peak MS. Philos Mag B – Phys Condens Matter Stat Mech Electron Opt Magn Prop 1984;49:295.
[9] Bhattacharya K. Microstructure of martensite: why it forms and how it gives rise to the shape-memory effect. Oxford: Oxford University Press; 2003.
[10] International tables for crystallography. Chester: International Union of Crystallography; 2006.
[11] Christian JW, Mahajan S. Prog Mater Sci 1995;39:1.
[12] Pond RC, Muntifering B, Müllner P. Acta Mater 2012;60:3976.
[13] Zarubova N, Ge Y, Gemperlova J, Gemperle A, Hannula SP. Funct Mater Lett 2012;5.
[14] Zarubova N, Ge Y, Heczko O, Hannula SP. Acta Mater 2013;61:5290.
[15] Kellis D, Smith A, Ullakko K, Müllner P. J Cryst Growth 2012;359:64.
[16] Kovarik L, Unocic RR, Li J, Sarosi P, Shen C, Wang Y, et al. Prog Mater Sci 2009;54:839.
[17] Pond RC. J Microsc – Oxford 1979;116:105.
[18] Pond RC. Interface Sci 1995;2:299.
[19] Cong DY, Zhang YD, Wang YD, Humbert M, Zhao X, Watanabe T, et al. Acta Mater 2007;55:4731.
[20] Wayman CM. Introduction to the crystallography of martensitic transformations. New York: Macmillan; 1964.
[21] Romanov AE, Wagner T. Scripta Mater 2001;45:325.
[22] Hirth JP, Pond RC. Philos Mag 2010;90:3129.
[23] Chernenko VA, Pons J, Segui C, Cesari E. Acta Mater 2002;50:53.
[24] Stuhr U, Vorderwisch P, Kokorin VV. J Phys-Condens Matter 2000;12:7541.
[25] Pond RC, Ma X, Chai YW, Hirth JP. In: Nabarro FRN, Hirth JP, editors. Dislocations in solids, vol. 74. Amsterdam: Elsevier Science; 2007. p. 225.
[26] Sutton AP, Balluffi RW. Interfaces in crystalline materials. Oxford: Clarendon Press; 1995.
[27] Romanov AE, Vladimirov VI. In: Nabarro FRN, editor. Dislocations in solids, vol. 9. Amsterdam: Elsevier Science; 1992.
[28] Romanov AE, Kolesnikova AL. Prog Mater Sci 2009;54:740.
[29] Müllner P, King AH. Acta Mater 2010;58:5242.
[30] Romanov AE, Vojta A, Pompe W, Lefevre MJ, Speck JS. Phys Stat Solidi a – Appl Res 1999;172:225.
[31] Romanov AE, Lefevre MJ, Speck JS, Pompe W, Streiffer SK, Foster CM. J Appl Phys 1998;83:2754.
[32] Speck JS, Daykin AC, Seifert A, Romanov AE, Pompe W. J Appl Phys 1995;78:1696.
[33] Straka L, Soroka A, Seiner H, Hanninen H, Sozinov A. Scripta Mater 2012;67:25.